

Forecasts of effects of beam systematics and deprojection on the third generation ground-based CMB experiment

Jiazheng Dou^{1,2*}, Jiakang Han^{3,4}, Wen Zhao^{1,2**}, and Bin Hu^{5,6***}

¹ Department of Astronomy, University of Science and Technology of China, Chinese Academy of Sciences, Hefei, Anhui 230026, People's Republic of China

² School of Astronomy and Space Sciences, University of Science and Technology of China, Hefei 230026, People's Republic of China

³ Dipartimento di Fisica, Università degli Studi di Torino, Via P. Giuria 1, 10125 Torino, Italy

⁴ INFN – Istituto Nazionale di Fisica Nucleare, Sezione di Torino, Via P. Giuria 1, 10125 Torino, Italy

⁵ Institute for Frontier in Astronomy and Astrophysics, Beijing Normal University, Beijing, 102206, People's Republic of China

⁶ Department of Astronomy, Beijing Normal University, Beijing 100875, People's Republic of China

December 31, 2024

ABSTRACT

The ground-based Cosmic Microwave Background experiments are susceptible to various instrumental errors, especially for B -mode measurements. The difference between the response of two polarized detectors, referred to as the “beam mismatch”, would induce a $T \rightarrow P$ leakage when differencing the detector pair to cancel the unpolarized signal. In this work, we apply the deprojection technique on the time-ordered mock data to mitigate the systematic contamination caused by beam mismatches, by assuming the third generation ground-based CMB experiment (S3). Our results show that the deprojection could effectively recover the input power spectra. We adopt the NILC and cILC methods to reconstruct the foreground-cleaned TEB maps, and evaluate the level of residual systematic errors after the foreground cleaning pipeline by comparing the power spectra between the systematics-added data after deprojection and the systematics-free data. The results demonstrate that the residual beam systematics cleaned by deprojection would not bias the CMB measurements of T , E , and B modes, as well as the CMB lensing reconstruction and the estimation of the tensor-to-scalar ratio under the S3 sensitivity.

Key words. Cosmic background radiation – Instrumentation: detectors – Gravitational lensing: weak

1. Introduction

The precise measurements of cosmic microwave background (CMB) polarization are particularly essential for modern cosmology and exploring new physics beyond the Λ CDM model (Planck Collaboration et al. 2020a). The detection of the primordial B -mode polarization would reveal the mystery of the cosmic inflation era. The amplitude of the primordial B modes is commonly described by the ratio of the tensor power spectrum to the scalar power spectrum at some pivot scale, named the tensor-to-scalar ratio. Successive ground-based CMB experiments over the past decade have made great efforts to increase their sensitivities to make a significant detection of the tensor-to-scalar ratio, such as BICEP/Keck (BICEP/Keck Collaboration et al. 2021), ACTpol (Louis et al. 2017), CLASS (Harrington et al. 2016), and SPTpol (Sayre et al. 2020). The current best constraint on the tensor-to-scalar ratio is $r < 0.032$ (95% C.L.) obtained from the combination of Planck, BAO, and BICEP/Keck data (Tristram et al. 2022). The future CMB experiments such as AliCPT (Li et al. 2019, 2018), Simons Observatory (Simons Observatory Collaboration et al. 2019), QUBIC (Mennella et al. 2019), LiteBIRD (Hazumi et al. 2019), and CMB-S4 (Abazajian et al. 2016, 2022; CMB-S4 Collaboration et al. 2022) will continue to pursue the target of higher sensitivities on constraining r .

The precise measurements of CMB polarization are challenging not only because of its weakness compared to the instrumental noise, but also due to the existence of complicated contaminants from both astrophysics and instruments. Diffuse galactic foregrounds such as synchrotron and thermal dust emit strong polarized radiation at microwave frequency bands with a significant amplitude relative to the CMB polarization signal. Component separation methods are implemented on the multi-frequency sky observations to remove the foregrounds (mostly) based on the fact that CMB and foregrounds have different spectral energy distributions (SED). Imperfect knowledge of the actual optical response of the telescopes results in instrumental systematic effects, such as the unknown difference between the response of two polarized detectors that might transform a fraction of CMB temperature modes into polarization modes, named the $T \rightarrow P$ leakage. The leakage must be mitigated especially because the temperature modes and the polarization modes peak at similar angular scales so that the former's leakage is of magnitude higher than the latter's signal. Additionally, the gravitational lensing effect where the matter field gravitationally deflects the CMB photons can convert part of E modes into B modes at intermediate and small scales, giving rise to lensing B modes which predominate over the primordial B modes (Blanchard & Schneider 1987; Zaldarriaga & Seljak 1998). Fortunately, the lensing convergence can be reconstructed using either internal CMB anisotropies or external large scale structure (LSS) tracers such as galaxy surveys, 21 cm observations, and Cosmic Infrared

* e-mail: doujzh@mail.ustc.edu.cn

** e-mail: wzhao7@ustc.edu.cn

*** e-mail: bhu@bnu.edu.cn

Background (CIB) measurements (Hu 2001; Hu & Okamoto 2002; Okamoto & Hu 2003; Carron & Lewis 2017; Maniyar et al. 2021; Planck Collaboration et al. 2019).

In this work, we consider a typical configuration for a small-aperture, ground-based CMB telescope. Specifically, we assume a total of 7,000 polarized detectors, evenly split between the 95 GHz and 150 GHz frequency bands. Each detector has a noise equivalent temperature (NET) of $350 \mu\text{K} \sqrt{s}$. The full width at half maximum (FWHM) beam sizes are assumed to be 19 arcminutes and 11 arcminutes for the 95 GHz and 150 GHz bands, respectively. This setup reflects the typical design of a third-generation ground-based CMB experiment (S3) (Abazajian et al. 2016). In this paper, we focus on exploring the impact of the beam mismatch, a difference in the beam shape or beam center between the two detectors of a detector pair that leads to the $T \rightarrow P$ leakage. An analysis technique dubbed the ‘‘deprojection’’ has been exploited to filter out this contamination (BICEP2 Collaboration et al. 2015; Sheehy 2019). We use the deprojection algorithm to handle the time-ordered data with the beam systematics added, and evaluate the effects of undeprojected residual systematics on the follow-up steps of our whole pipeline, including component separation, lensing reconstruction, and the estimation of the tensor-to-scalar ratio. The residual systematic error is found to be negligible given the sensitivity of S3.

The paper is organized as follows. In Sect. 2 we first review the formalism of beam mismatches modeled by six coefficients. Then, we introduce our deprojection pipeline to mitigate the systematics induced by beam mismatches. Finally, we summarize the simulations used to assess the effectiveness of deprojection. In Sect. 3 we introduce the foreground cleaning pipelines including NILC and cILC, used for cleaning T/E modes and B modes respectively. We present the results of the mock data after deprojection and foreground cleaning, carry out a lensing reconstruction process on the foreground-cleaned maps, and constrain the tensor-to-scalar ratio r using the cleaned B -mode power spectrum in Sect. 4. Finally we conclude in Sect. 5.

2. Beam systematics and deprojection

Beam is the response of an antenna to sky radiation as a function of angle. Basically each pixel on the focal plane includes a pair of two orthogonally polarized antennas that observe the same direction on the sky. The time-ordered data (TOD) from detectors a and b (a pair) are summed to obtain the total intensity (temperature) measurement and differenced to cancel the unpolarized component thus measuring the polarization of radiation. The typical beams of S3 are circular Gaussians with FWHM = 19 arcmin for 95 GHz, and 11 arcmin for 150 GHz, where there is no systematics in the ideal case. However, if the beams of the two antennas are mismatched, which means their instrumental responses are different, the temperature signal is not completely canceled and could induce a spurious polarization signal into the pair difference data of the detector pair.¹ For the i -th detector, the TOD stream reads

$$\begin{aligned} \tau_i(t) = g_i \int d\nu \int d\Omega' A_i(\nu) B_i[\hat{n}(t) - \hat{n}'] \\ [L'_\nu(\hat{n}') + Q'_\nu(\hat{n}') \cos 2\psi_i(t) + U'_\nu(\hat{n}') \sin 2\psi_i(t)]. \end{aligned} \quad (1)$$

¹ If the beams of both detectors within a pair are identically distorted, the total miscalibration effect would not induce the $T \rightarrow P$ leakage but other systematics instead (BICEP/Keck Collaboration et al. 2023). Several filtering systematics that may cause the $E \rightarrow B$ leakage have been discussed in Ghosh et al. (2022).

Among them, g_i is the gain of the detector, $A_i(\nu)$ is the response of this detector at different frequencies, and $B_i[\hat{n}(t) - \hat{n}']$ is the beam function, representing the spatial response of the detector. $[I, Q, U](\hat{n}, \nu)$ are the Stokes parameters of the cosmic microwave background radiation at frequency ν and position \hat{n} . The terms $\hat{n}(t)$ and $\psi_i(t)$ are determined by the scan strategy. In an ideal case, both $B(\hat{n})$ and $A_i(\nu)$ are delta functions. The beam systematic errors are included in the following way.

1. Pointing error, this refers to the deviation between the pointing direction read by the instrument \hat{n}_{Ins} and the true pointing direction of the telescope \hat{n} .
2. Band pass mismatch, for a pair of detectors a and b , band pass mismatch means $A_a(\nu) \neq A_b(\nu)$, which can introduce false signals when taking the difference between the readings of the detectors.
3. Beam mismatch, similarly, for a pair of detectors a and b , beam mismatch refers to $B_a(r) \neq B_b(r)$, which can also introduce false signals in the detector difference.
4. Gain mismatch, when $g_a \neq g_b$, it is referred to as gain mismatch. Like the previous two points, this can introduce false signals in the detector difference.
5. Detector polarization angle calibration error, typically, the polarization directions detected by two detectors are set to an angle of 90° . However, due to the precision of the detector’s manufacturing, there can be a deviation in the preferred polarization angle, that is, $\psi_a(t) - \psi_b(t) \neq 90^\circ$, which can introduce systematic errors during the subsequent map-making process.

The first four errors above are all equivalent to an overall miscalibration of detectors and a differential response between a pair of detectors at the same frequency, where we refer to the latter as ‘‘beam mismatch’’ in the following. The detector polarization angle miscalibration would introduce the $E \rightarrow B$ leakage, which is beyond the scope of this work. Given the high amplitude of CMB temperature anisotropies relative to the polarization signal, the leakage from T to P must be carefully taken into account. The $T \rightarrow P$ leakage due to beam mismatches can be written as the convolution of the unpolarized signal and the differential beam within a detector pair

$$d_{T \rightarrow P} = T(\hat{n}) * [B_a(\hat{n}) - B_b(\hat{n})] = T(\hat{n}) * B_\delta(\hat{n}), \quad (2)$$

where $T(\hat{n})$ refers to the temperature anisotropies, $B_a(\hat{n})$ and $B_b(\hat{n})$ are the beams of two detectors, and $B_\delta(\hat{n})$ is the pair’s differential beam.

As in BICEP2 Collaboration et al. (2015) (hereafter BKIII), we model $B_\delta(\hat{n})$ as the difference of two elliptical Gaussian beams for simplicity, which can be parameterized by six parameters (or differential modes): the gain difference δg , the differences of pointing center coordinates (with respect to the nominal beam center) δx and δy , the Gaussian beamwidth difference $\delta\sigma$, and the differences of plus- and cross-ellipticity δp and δc . Plus- or cross-ellipticity describes an ellipse with its major axis oriented either horizontally/vertically or $\pm 45^\circ$ with respect to the x -axis (see more details in Appendix A of BKIII). For each differential mode $k = \{g, x, y, \sigma, p, c\}$, $\delta k = k_a - k_b$ is the difference of the beam parameter between two detectors. $B_\delta(\hat{n})$ is the linear combination of the beams of the six modes, where each mode independently produces a pattern of the spurious polarized signal, also named a ‘‘leakage template’’. For instance, since the beam of differential gain $B_{\delta g}(\hat{n})$ is simply the scaled version of the circular Gaussian beam, its leakage is simply the scaled version of the beam-smoothed temperature $\tilde{T}(\hat{n})$, from Eq. (2). Under the

Table 1: The six beam mismatch parameters added to the mock data and the corresponding leakage templates.

Mode	Gain	Beamwidth	Pointing, x	Pointing, y	Ellipticity, +	Ellipticity, ×
Symbol	δg	$\delta\sigma$	δx	δy	δp	δc
Template ^a	\tilde{T}	$(\nabla_x^2 + \nabla_y^2)\tilde{T}$	$\nabla_x\tilde{T}$	$\nabla_y\tilde{T}$	$(\nabla_x^2 - \nabla_y^2)\tilde{T}$	$2\nabla_x\nabla_y\tilde{T}$
95GHz mean	3.9×10^{-4}	$-0.0026'$	$-0.9'$	$0.72'$	4.3×10^{-3}	-8.9×10^{-3}
95GHz std	3×10^{-3}	$0.072'$	$0.35'$	$0.29'$	1.4×10^{-2}	1.3×10^{-2}
150GHz mean	2.7×10^{-4}	$-0.0043'$	$-0.9'$	$0.84'$	2.5×10^{-3}	-3.2×10^{-3}
150GHz std	3×10^{-3}	$0.072'$	$0.39'$	$0.35'$	1.5×10^{-2}	1.5×10^{-2}

(a)

\tilde{T} is the temperature field convolved by the nominal beam. All six templates are \tilde{T} and its first and second derivatives.

assumption that the mismatch is small, saving up to second order, all the templates are the beam-smoothed map of $T(\hat{n})$ and its first and second spatial derivatives (see Table 1) (Hu et al. 2003). The mapmaking procedure is a linear operation, meaning that the total leakage is the linear combination of the leakage templates of these differential modes. Therefore, we can filter out the leakage by fitting these templates to our data, and then subtracting them.

The leakage templates we use are from the Planck 100 and 143 GHz re-observed time-ordered data, used to clean 95 and 150 GHz respectively. The re-observed templates are produced by:

1. First generate CMB, foreground and noise simulations of Planck HFI bands as introduced below.
2. Co-add all components and reconvolve the co-added sky maps with the S3 nominal beams. For Planck 100 GHz, we divide the a_{tm} 's by the 100 GHz beam function and then multiply them by the S3 95 GHz Gaussian beam. (This can be done on the input maps since both Planck and S3 nominal beams are circularly symmetric.)
3. Compute the first and second derivatives of the Planck T maps.²
4. Re-scan the T maps and their derivatives for each HFI band using the same pointing matrix as in S3.

For the realistic observations, we will “re-observe” PR4 (NPIPE) maps (Planck Collaboration et al. 2020b) using the S3 scan strategy. Our templates contain the noise component of Planck HFI bands that is not involved in the true $T \rightarrow P$ leakage, but we assume the noise is small compared to the temperature signal. We produce simulated S3 TOD from CMB-plus-foregrounds co-added maps using Eq. (1), and compute the pair difference time stream of the TOD by differencing the a and b detector time streams within a pair: $\tau_{\text{diff}}(t) = (\tau_a - \tau_b)(t)/2$. Lastly, we fit the templates to the pair difference TOD and subtract the fitted templates. Noise is not involved in the data since we expect the noise uncorrelated to the templates from Planck HFI maps, and the separation of noise ensures clearer analyses of different components in the following foreground cleaning pipeline.

The assumed S3 experiment is located in the northern hemisphere. In its first observing season, it will scan 17% of the sky where the thermal dust emission is clean, centering at RA = 170° and DEC = 40° in the celestial coordinate system. The polarized

maps have a map depth of about 18 μK -arcmin at 95 GHz and 24 μK -arcmin at 150 GHz.

Our mock dataset consists of 300 simulated sky maps at $N_{\text{side}} = 1024$ in seven frequency bands, including 95 and 150 GHz dual bands, Planck HFI 100, 143, 217, 353 GHz bands, and WMAP K band. The additional Planck and WMAP channels are for the purpose of cleaning foregrounds more thoroughly. Each of the sky maps contains CMB, foregrounds, and white noise. First, we draw the six ΛCDM cosmological parameters within one standard deviation of the Planck 2018's best-fit cosmological constraints (Planck Collaboration et al. 2020a), from which we generate the lensed CMB power spectrum by CAMB (Lewis et al. 2000). The CMB realizations are generated from the lensed power spectrum with the tensor-to-scalar ratio $r = 0$, using **synfast** facility from **lenspyx** (Reinecke et al. 2023). The Galactic foregrounds containing thermal dust, synchrotron, free-free, spinning dust and CO emissions are produced using the Planck Sky Model (PSM) package (Delabrouille et al. 2013), which are the same as the foregrounds used in previous papers (Dou et al. 2024; Han et al. 2023b). The thermal dust polarization maps are generated by scaling the Planck 2018 GNILC polarized dust template (Planck Collaboration et al. 2020c) to different frequencies using a modified blackbody SED with dust temperature and spectral indices adopted from the best fit of Planck 2015 GNILC dust maps (Planck Collaboration et al. 2016). The synchrotron polarization template is based on the Planck 2018 SMICA map, and is scaled by a power law SED with a fixed β_s of -3.08. We do not use the current best-fit values to avoid confirmation biases during foreground removal. For only 95 and 150 GHz bands, we generate the TOD simulations of CMB plus foregrounds following Eq. (1) and the S3 scan strategy, where we assume the stochastic beam mismatch parameters whose mean and uncertainty are listed in Table 1. The values are chosen to be at the same level with the measured beam parameters of BICEP2 instruments (BICEP2 Collaboration et al. 2014; BICEP2/Keck Collaboration et al. 2015). They measured the beam shape parameters for each detector using a chopped thermal source mounted on a mast, and calibrated the differential gains using the cross-correlation of temperature maps for individual detectors with Planck. We create white noise simulations assuming that the realistic $1/f$ noise could be significantly removed by pair differencing and TOD polynomial filtering (BICEP2 Collaboration et al. 2014). The white noises unrelated to systematics are generated from the noise covariance matrices of S3 and WMAP-K bands (Bennett et al. 2013). For Planck HFI bands, we adopt 300 FFP10 noise simulations from the Planck Legacy

² Although the deprojection technique is implemented on time streams of partial-sky observations, the computation of the first and second derivatives of T maps is performed on Planck full-sky simulated data, thus being immune to the patch's borders effects.

Archive³. The deprojection process is performed on the CMB-plus-foregrounds data assuming it makes negligible effects on the noise component.

3. Foreground cleaning pipeline

In this paper, we implement the same foreground cleaning methods as Han et al. (2023b) to qualify the performance of deprojection on the foreground-cleaned maps. The T and E modes are cleaned by the NILC method, and the B modes are cleaned by the cILC method due to the dominance of foregrounds over the B -mode signal.

The maps after foreground cleaning (NILC or cILC) consist of four ingredients: the CMB signal, the residual foregrounds, the residual noise and the systematic residual. Theoretically, for the purpose of examining the efficacy of the foreground cleaning methods, each component in the output map can be obtained by projecting ILC weights on the maps of the input component, given the linearity of ILC methods. However, the input CMB and foregrounds are mixed up during deprojection so that the systematic contamination on the CMB and foregrounds can never be separated afterward. Instead, we first subtract the residual noise from the total residual (the foreground-cleaned map minus the input CMB map), which turns out to be the sum of residual foregrounds and the systematic residual. We then project the ILC weights on the deprojection residual maps at 95 and 150 GHz bands to obtain the deprojection residual in the foreground-cleaned maps. Finally we subtract it from the sum to compute the residual foregrounds.

3.1. The NILC pipeline

The needlet internal linear combination (NILC) method (Delabrouille et al. 2009; Basak & Delabrouille 2012, 2013) is a widely used blind component separation technique that linearly combine the raw data from different frequencies while minimizing the variance in the needlet space. Needlets are a special form of wavelets that permit localization in both harmonic and real/pixel space, making itself suitable for component separation where the properties of sky components vary significantly with both sky positions and scales. In this work, we adopt the NILC method for cleaning foregrounds in T - and E -mode maps, the details of which are as follows.

The sky observations $d_\nu(p)$ at a frequency band ν and sky pixel p are first transformed into spherical harmonic coefficients using HEALPix⁴ (Gorski et al. 2005): $d_{\ell m}^\nu = \int d_\nu(p) Y_{\ell m}^*(p) d\Omega$. The raw maps with different beams are then reconvolved into the common resolution by $d_{\ell m}^{\nu, \text{out}} = d_{\ell m}^{\nu, \text{in}} b_\ell^{\text{out}} / b_\ell^{\text{in}}$, where b_ℓ is the beam transfer function. The common beam resolution (b_ℓ^{out}) is chosen as the Gaussian beam of FWHM=11 arcmin, which is the resolution of 150 GHz band. For WMAP K band and 95 GHz that have larger beam sizes than the common beam ($b_\ell^{\text{in}} < b_\ell^{\text{out}}$), we cut off the harmonic coefficients of these two bands with ℓ greater than 350 and 1200, respectively, to avoid overamplification of the instrumental noise. The harmonic coefficients can be decomposed into a set of filtered maps:

$$d_{\ell m}^{\nu, j} = h_\ell^j d_{\ell m}^\nu, \quad (3)$$

where the needlet bands h_ℓ^j satisfy $\sum_j (h_\ell^j)^2 = 1$, defining a localization scheme in harmonic space. In this work we adopt the

cosine needlet bands as shown in Fig. 1 of Han et al. (2023b). The 8 needlet bands peak at 15, 30, 60, 120, 300, 700, 1200 and 2000 respectively with $\ell_{\text{max}} = 2000$. Note for WMAP K band whose coefficients with $\ell > 350$ are cut off, the needlets whose peaks (ℓ_{peak}) are greater than 350 would not be applied to the K band data (and so is for 95 GHz band). For each frequency band, the filtered maps are then transformed back to real space, forming a set of needlet maps. The needlet coefficient of the j -th needlet and the k -th pixel after transformation is given by:

$$b_j^\nu(\hat{p}_{jk}) = \sqrt{\frac{4\pi}{N_j}} \sum_{\ell m} h_\ell^j d_{\ell m}^\nu Y_{\ell m}(\hat{p}_{jk}), \quad (4)$$

where N_j denotes the number of pixels of the j -th needlet map, and \hat{p}_{jk} denotes the pixel center of the k -th pixel of the j -th needlet map.

Once the data have been transformed to needlet space, we apply the internal linear combination method to the multichannel data. First we estimate the data covariance matrix across frequencies by averaging the needlet coefficient product $b_j^{\nu_1}(\hat{p}_{jk}) b_j^{\nu_2}(\hat{p}_{jk})$ over a disk of pixels centered at pixel k . The empirical data covariance between ν_1 and ν_2 is written as:

$$\hat{C}_{jk}^{\nu_1 \times \nu_2} = \frac{1}{n_k} \sum_{k'} w_j(k, k') b_j^{\nu_1}(\hat{p}_{jk'}) b_j^{\nu_2}(\hat{p}_{jk'}), \quad (5)$$

where $w_j(k, k')$ are the weights that select the region around pixel k to average out, and n_k is the number of selected pixels. The NILC solution is a linear combination of the needlet coefficients of all frequencies:

$$b_j^{\text{NILC}}(\hat{p}_{jk}) = \sum_\nu w_{\nu, j}^{\text{NILC}}(\hat{p}_{jk}) b_j^\nu(\hat{p}_{jk}), \quad (6)$$

where the NILC weights are given by:

$$w_{\nu, j}^{\text{NILC}}(\hat{p}_{jk}) = \left[\hat{C}_{jk}^{-1} \mathbf{a} \right]_{\nu} \cdot \left[\mathbf{a}' \hat{C}_{jk}^{-1} \mathbf{a} \right]_{\nu}^{-1}. \quad (7)$$

Here \hat{C}_{jk} is the $n_\nu \times n_\nu$ empirical data covariance matrix where n_ν is the number of frequency channels, and \mathbf{a} is the spectral response vector that characterizes how the signal varies with frequencies. Given that the CMB signal is frequency independent in thermodynamic temperature units, we set \mathbf{a} as a unit column vector with length of n_ν . The relation $\sum_\nu a_\nu w_{\nu, j}^{\text{NILC}} = 1$ ensures the precise recovery of the CMB component.

Finally we do inverse needlet transformation to obtain the NILC cleaned map:

$$\hat{s}_{\ell m}^{\text{NILC}} = \sum_{jk} b_j^{\text{NILC}}(\hat{p}_{jk}) \sqrt{\frac{4\pi}{N_j}} h_\ell^j Y_{\ell m}(\hat{p}_{jk}). \quad (8)$$

The recovered CMB map in real space is given by $\hat{s}_{\text{NILC}}(p) = \sum_{\ell m} \hat{s}_{\ell m}^{\text{NILC}} Y_{\ell m}(p)$. We use a mask preserving the pixels with the noise variance of 150 GHz band smaller than $20 \mu\text{K}$ -pixel, whose sky fraction is about 10% (see Fig. 3).

3.2. The cILC pipeline

Following the ILC method, the constrained ILC (cILC) method (Remazeilles et al. 2011, 2021) is developed to further mitigate the residual foreground contaminants by adding constraints on

³ <http://pla.esac.esa.int/pla>

⁴ <http://healpix.sf.net/>

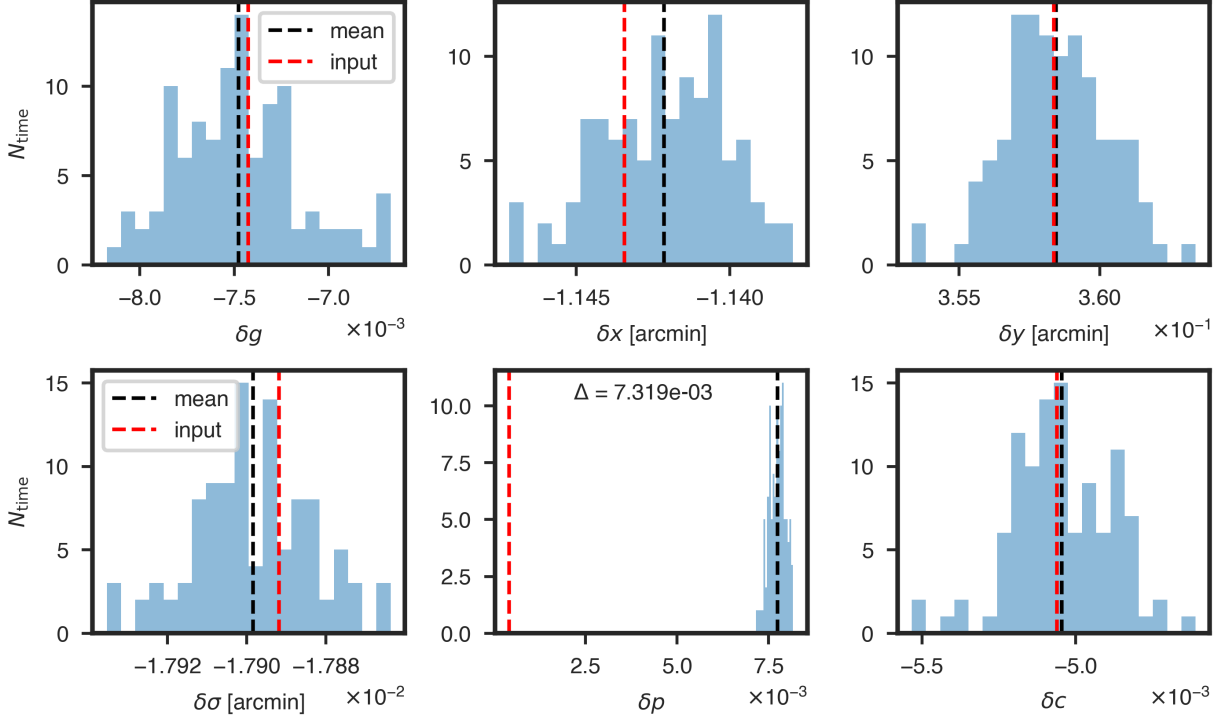


Fig. 1: Distribution of the recovered beam mismatch parameters of 106 time trunks for one detector pair of a noise-free simulation at 150 GHz. The red dashed lines represent the input beam parameter and the black dashed lines indicate the mean over all time series. There is a bias on the differential plus-ellipticity of $\Delta \approx 7.3 \times 10^{-3}$ due to the cosmological TE correlation.

the ILC weights. In this work, we use the cILC method in harmonic space to produce foreground cleaned B -mode maps, since the foregrounds are several orders of magnitude higher than the CMB signal for B modes, and thus the standard ILC method is insufficient to reduce the residual foregrounds to a level of $r = 0.01$ primordial tensor modes under the sensitivities of S3.

We model the B -mode observation at frequency ν and pixel p as the sum of n_c sky components and the thermal noise:

$$d_\nu(p) = \sum_c A_{\nu c} s_c(p) + n_\nu(p), \quad (9)$$

where $s_c(p)$ is the astrophysical emission template of component c and $n_\nu(p)$ is the noise. The $n_\nu \times n_c$ mixing matrix \mathbf{A} stores the spectral response information that describes the SED of component c at frequency ν . In our implementation we consider only three dominant sky components including the lensed CMB, the polarized thermal dust and the polarized synchrotron. The first column of the mixing matrix refers to the mixing vector of CMB, \mathbf{a} . The second column corresponding to dust emissions is calculated assuming a modified blackbody SED with fixed $T_{\text{dust}} = 19.6K$ and $\beta_{\text{dust}} = 1.59$. The third column, that is, the mixing vector of synchrotron follows the power law SED with fixed $\beta_{\text{sync}} = -3$ in Rayleigh-Jeans brightness temperature units.

The cILC weights are given by:

$$\mathbf{w}^{\text{cILC}} = \mathbf{e} \left(\mathbf{A}^T \hat{\mathbf{C}}^{-1} \mathbf{A} \right)^{-1} \mathbf{A}^T \hat{\mathbf{C}}^{-1}, \quad (10)$$

which satisfy the constraints nulling the foreground components (dust and synchrotron):

$$\sum_\nu w_{\nu, \ell}^{\text{cILC}} A_{\nu, c} = e_c, \quad (11)$$

where \mathbf{e} is a row vector with length n_c whose element e_c is 1 for CMB and 0 for foreground components. The empirical data covariance matrix $\hat{\mathbf{C}}$ is computed by:

$$\hat{\mathbf{C}}_\ell^{\nu_1 \times \nu_2} = \frac{1}{\sum_{\ell'=\ell_{\min}}^{\ell_{\max}} (2\ell+1)} \sum_{\ell'=\ell_{\min}}^{\ell_{\max}} \sum_{m=-\ell'}^{\ell'} d_{\ell'm}^{\nu_1*} d_{\ell'm}^{\nu_2}, \quad (12)$$

where $\ell_{\min} = \min[0.6\ell, \ell-7]$, $\ell_{\max} = \max[1.4\ell, \ell+7]$, and we exclude the center multipole ($\ell' \neq \ell$) to mitigate the ILC bias. The input maps are reconvolved to a common beam of 11 arcmin. The analysis is performed with $\ell_{\max} = 2000$, while the harmonic coefficients of WMAP-K and 95 GHz bands are not involved as ℓ is greater than 350 and 1200, respectively. The cILC cleaned CMB map is finally obtained by $\hat{s}_{\ell m}^{\text{cILC}} = \sum_\nu w_{\nu, \ell}^{\text{cILC}} d_{\nu, \ell m}$. To reduce the foreground contaminants, we use a smaller mask ($f_{\text{sky}} \approx 7\%$) for cleaning B maps, which is produced by removing the pixels with the noise variance of 150 GHz band larger than $10 \mu\text{K-pixel}$ and the declination above 65° (see the third row of Fig. 5).

4. Results

In this section, we detail the results of the fitted beam parameters from deprojection and the deprojected maps of S3 dual bands. We then combine the S3 channels with four Planck HFI channels and WMAP K band in the foreground cleaning pipeline to extract the CMB signal, and reconstruct the lensing potential power spectrum from the foreground-cleaned maps. We finally evaluate the impacts of the systematic residual on the CMB power spectra, lensing potential, and the tensor-to-scalar ratio r .

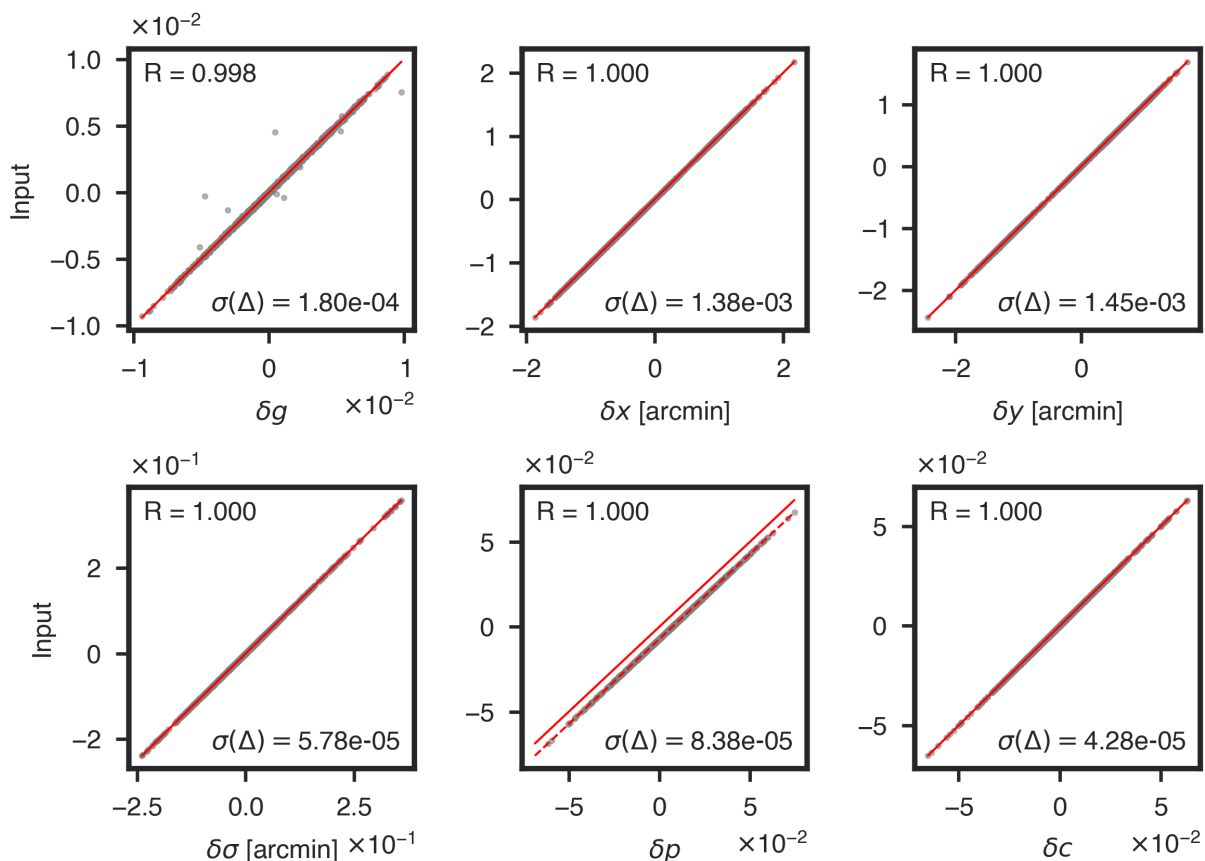


Fig. 2: Scatter plot of the recovered beam mismatch parameters averaged over time trunks (x -axis) vs. the input values (y -axis) for all 1728 detector pairs of a simulation at 150 GHz. The red solid curves have a slope of 1 and a y -intercept of 0. The red dashed curve has been offset vertically by the mean bias on δp estimated from systematics-free simulations. The correlation coefficient R and the standard deviation of the bias on the deprojection coefficient $\sigma(\Delta)$ are exhibited.

4.1. Deprojection results

The assumed S3 telescope contains 1728 detector pairs on the focal plane for both 95 and 150 GHz bands, with a field-of-view width $\sim 30^\circ$. We consider one observing season (lasting about half an year) which is divided into 3183 “scansets” (each lasting roughly 30 minutes). A scanset covers tens of constant elevation scans (CES) that the telescope operates from one end to the other at a speed of $\sim 4^\circ/s$. Between scansets, the telescope makes elevation nodding (elnod) scans to calibrate the relative gains of detectors. We generate time streams from simulated CMB plus foregrounds following the S3 scan trajectory. We derive the six leakage templates from Planck simulations as described in Sect. 2. Although the input beam parameters are constant with time, we fit the time-ordered templates to the S3 TOD every 30 scansets for each detector pair to account for the time-varying beam systematics in realistic instruments. The histogram of the fitted beam mismatch parameters of 106 time chunks for one detector pair of a realization at 150 GHz is shown in Fig. 1. The scatter across time slices would be averaged in the mapmaking process, and the deviation of the mean from the true values (input parameters) due to noise fluctuations in templates leads to the undeprojected residual.

We notice a systematic bias on the recovered differential plus-ellipticity δp at a level of $\Delta = \delta p_{\text{recov}} - \delta p_{\text{input}} \approx 7.3 \times 10^{-3}$. Due to the CMB inherent TE correlation, the deprojection tem-

plate of δp correlates with the polarized signal in the pair difference time stream, resulting in a bias on the deprojection coefficient even in the beam-systematics-free case (BICEP2 Collaboration et al. 2015). This bias does not impair the filtering of $T \rightarrow P$ leakage, but leads to additional filtering of cosmological E modes (the effects on B modes is negligible). We have corrected for the bias using the averaged deprojection coefficient estimated from systematics-free simulations, which is $\langle \delta p_{\text{recov}} \rangle = 7.2 \times 10^{-3}$.⁵

Figure 2 shows the comparison between the fitted beam mismatch parameters in deprojection and the input values for 1728 detector pairs of a realization at 150 GHz. The red solid curves refer to $y = x$, and the red dashed curve has been vertically offset by the estimated mean bias on δp (7.2×10^{-3}). The Pearson correlation coefficient R approaching 1 for all parameters indicates a strong correlation between the deprojection coefficients and the input parameters, demonstrating the precision of deprojection. The standard deviation of the bias (Δ) on each coefficient is significantly lower than the median measurement uncertainty for individual detectors by BICEP2/Keck Array (see Table 3 of BICEP2/Keck Collaboration et al. (2015)), but is too optimistic since the noise is not added to the data.

⁵ The bias can be alternatively taken into account in the final power spectrum by a suppression factor on E modes derived from the deprojected systematics-free simulations.

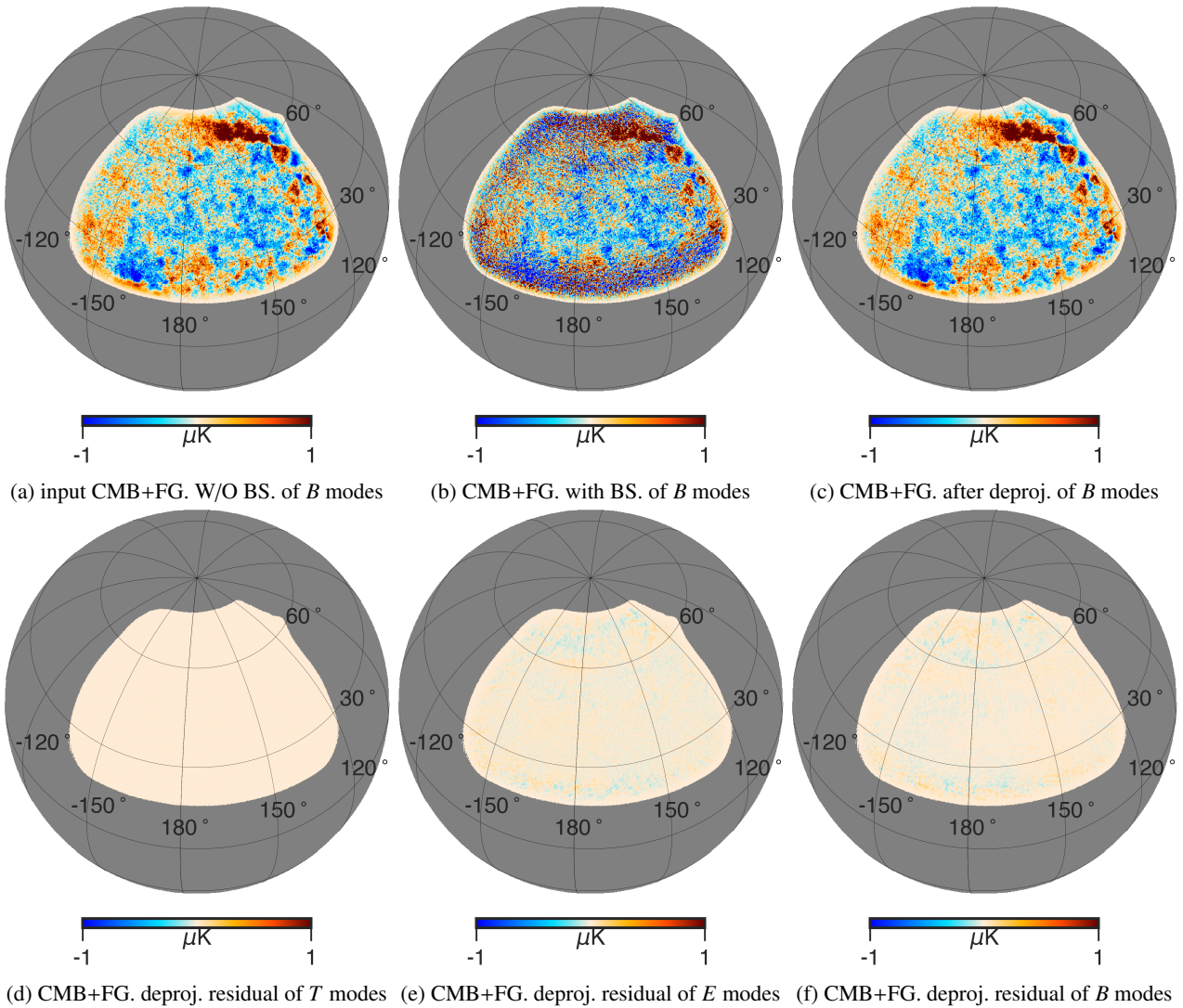


Fig. 3: Maps of CMB plus foregrounds at S3 150 GHz. First row: the input B -mode CMB and foregrounds without beam systematics (left), the CMB plus foregrounds with beam systematics (middle) and after deprojection (right). Second row: the difference between the deprojected map and the input map without beam systematics for T (left), E (middle) and B (right) modes. The results of 95 GHz are similar to the 150 GHz results.

Finally, we subtract the fitted templates from the pair difference data for all time trunks of detector pairs. We simplify the mapmaking process by averaging the time streams of detectors pointed at each map pixel and adding white noise maps to obtain the observed sky maps.

4.2. Frequency maps

We perform the deprojection procedure on CMB-plus-foregrounds TOD with beam systematics of S3 95 and 150 GHz bands and implement the mapmaking to obtain the frequency maps. The 150 GHz B -mode maps before and after the deprojection pipeline are plotted in the first row of Fig. 3, where the left plot shows the input CMB plus foregrounds without beam systematics, the middle plot shows the CMB plus foregrounds with beam systematics, and the right plot shows that after deprojection. The beam systematics with the level considered in this work only make substantial effects on B modes, which induce a spurious signal mainly at small scales. The deprojection residual maps shown in the second row of Fig. 3 illustrate the capability

of deprojection to recover the input $T/E/B$ signal. The deprojection has nothing to do on T modes, but the noise fluctuation in the deprojection template may lead to a residual T -to- P leakage on E and B modes. However, our results show that the residual leakage almost vanishes in deprojected maps.

We use the PCL-TC estimator (as detailed in Appendix A) to estimate the power spectra of 150 GHz maps, as shown in Fig. 4. The bandpowers have a multipole bin size of 30 and $\ell_{\max} = 700$. Only in BB power spectrum could the beam systematics bias the power spectrum of input CMB plus foregrounds significantly, while the power spectra of deprojected maps for all modes fit well with the input spectra. The residual after deprojection (plotted in cyan dashed curves) for BB is about 2~3 orders of magnitude lower than the input CMB plus foregrounds power spectrum (black solid curves).

4.3. Foreground-cleaned maps

After propagating the maps with beam systematics through the deprojection pipeline, we use the NILC method to clean fore-

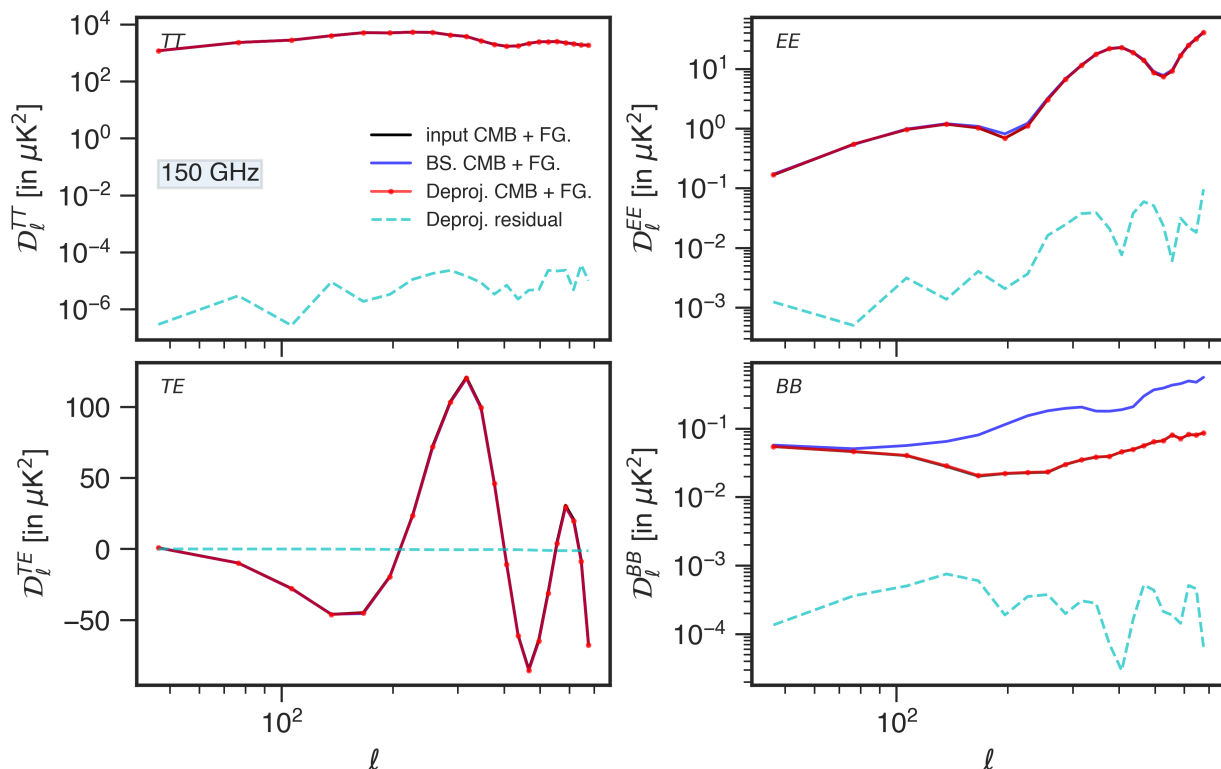


Fig. 4: TT , EE , TE and BB power spectra of the 150 GHz CMB plus foregrounds map with beam systematics before (blue curves) and after deprojection (red curves) for one realization. The input CMB+FG. power spectrum without beam systematics is shown in black solid curves for comparison with the deprojected one, and their difference, the residual after deprojection is shown in cyan dashed curves. The results of 95 GHz are similar to the 150 GHz results.

grounds of T - and E -mode maps, and use the cILC approach to clean B -mode maps. The cleaned maps are plotted in Fig. 5. The left column shows the input CMB maps without adding beam systematics, the middle column shows the NILC-cleaned T and E maps from seven bands, and the right column shows the difference between the cleaned map and the input CMB. The residual maps are dominated by the noise fluctuation for B modes, while the NILC maps for T and E modes are signal-dominated.

For B modes, we compute the systematic residual map by projecting the cILC weights on the 95 and 150 GHz deprojection residual maps plotted in Fig. 3. In such a way, we separate the three components in the B -mode cILC residual map from each other, as shown in Fig. 6. We can see the small-scale artifacts presented in the systematic contamination map. The residual on the boundaries would be removed through mask apodization in the power spectrum estimation.

The power spectra of NILC and cILC reconstructed maps are shown in Fig. 7. The orange curves refer to the residual noise power spectrum obtained from projecting the NILC or cILC weights on the input noise maps. The green curves, as mentioned in Sect. 3, represent the sum of the foreground and beam systematic residuals. For B modes, the two contaminant components are separately plotted in red and purple curves. The foreground residual dominates the systematic residual at large scales ($\ell \lesssim 300$). The deprojection residual is negligible compared to the CMB B -mode power spectrum at all scales. Our foreground cleaning methods are sufficient to recover the CMB signal with the residual contaminants remaining much lower than the reconstructed CMB power spectrum for T and E modes, and than the noise fluctuation for B modes.

4.4. Lensing reconstruction

Thanks to the excellent noise performance, besides of the primordial B -mode signal, S3 can also detect the lensing signal with a moderate significance. In what follows we evaluate the systematic effects on the lensing reconstruction by using the simulated 4 modules*yr data. We feed 301 sets of simulations mentioned above through the lensing pipelines (Carron & Lewis 2017; Liu et al. 2022a; Han et al. 2023a) and test their performance.

In the presence of lensing-induced correlations among different multipole moments, the off-diagonal terms of the covariance matrix of the CMB fields become nonzero. This allows us to calculate the quadratic estimator (Hu & Okamoto 2002; Okamoto & Hu 2003) using pairs of filtered maps in their quadratic form (Carron & Lewis 2017; Maniyar et al. 2021), as described in Eqs. (3.4) to (3.8) of Liu et al. (2022b). In this approach, one map in the pair is Wiener-filtered, while the other is inverse-variance filtered. To mitigate biases introduced by random disconnected noise, masking effects and foreground residuals, we employ a Monte Carlo simulation method to estimate these contributions and perform mean-field subtraction by averaging over the quadratic estimators, using 60 simulation sets.

Normalization is conducted in two stages: first, we assess the averaged noise level across the entire mock dataset and compute the normalization factor analytically, assuming an effective isotropic noise level. Then we correct for normalization bias arising from noise inhomogeneities through numerical simulations. The raw power spectrum of the lensing is simply

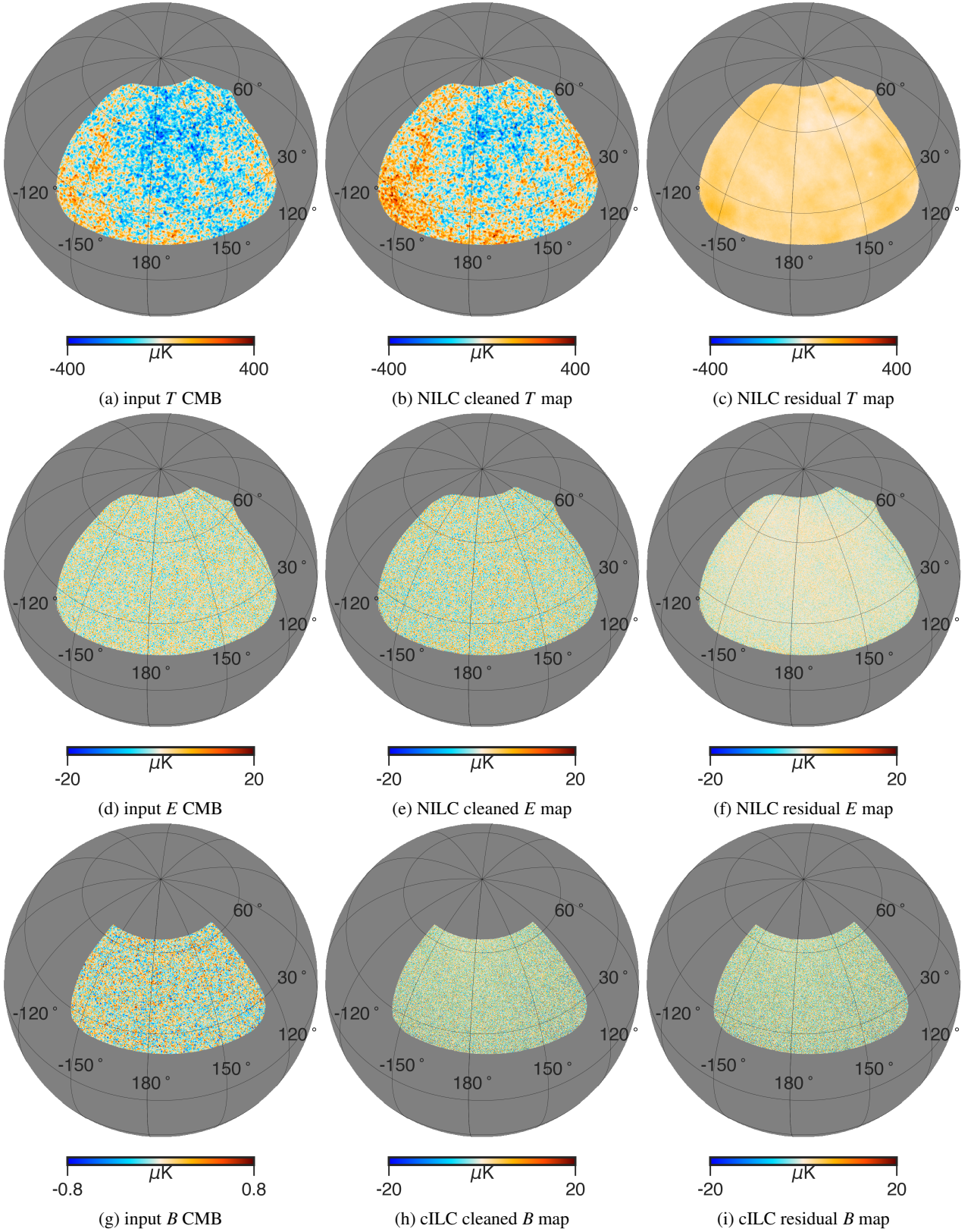


Fig. 5: Maps of the input CMB (left column), the foreground cleaned maps (middle column) and their difference, that is, the residual maps (right column) for T , E , and B modes. The first row shows T maps, the second row shows E maps and the third row shows B maps.

$$\hat{C}_L^{\hat{\phi}\hat{\phi}} = \frac{1}{(2L+1)f_{\text{sky}}} \sum_{M=-L}^L \hat{\phi}_{LM} \hat{\phi}_{LM}^*,$$

(13) where $\hat{\phi}_{LM}$ denotes the harmonic transformation of the reconstructed lensing potential. However, the outcome of the quadratic estimator contains not only the lensing potential signal but also

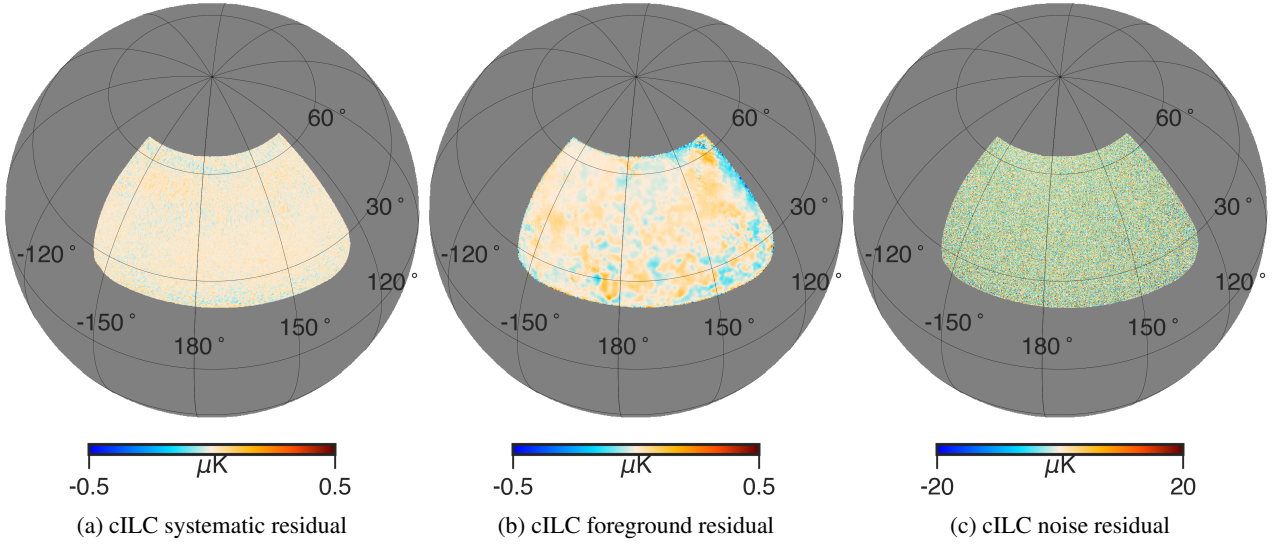


Fig. 6: cILC residual B maps of the systematics (left), foregrounds (middle) and noise (right) components, for one realization.

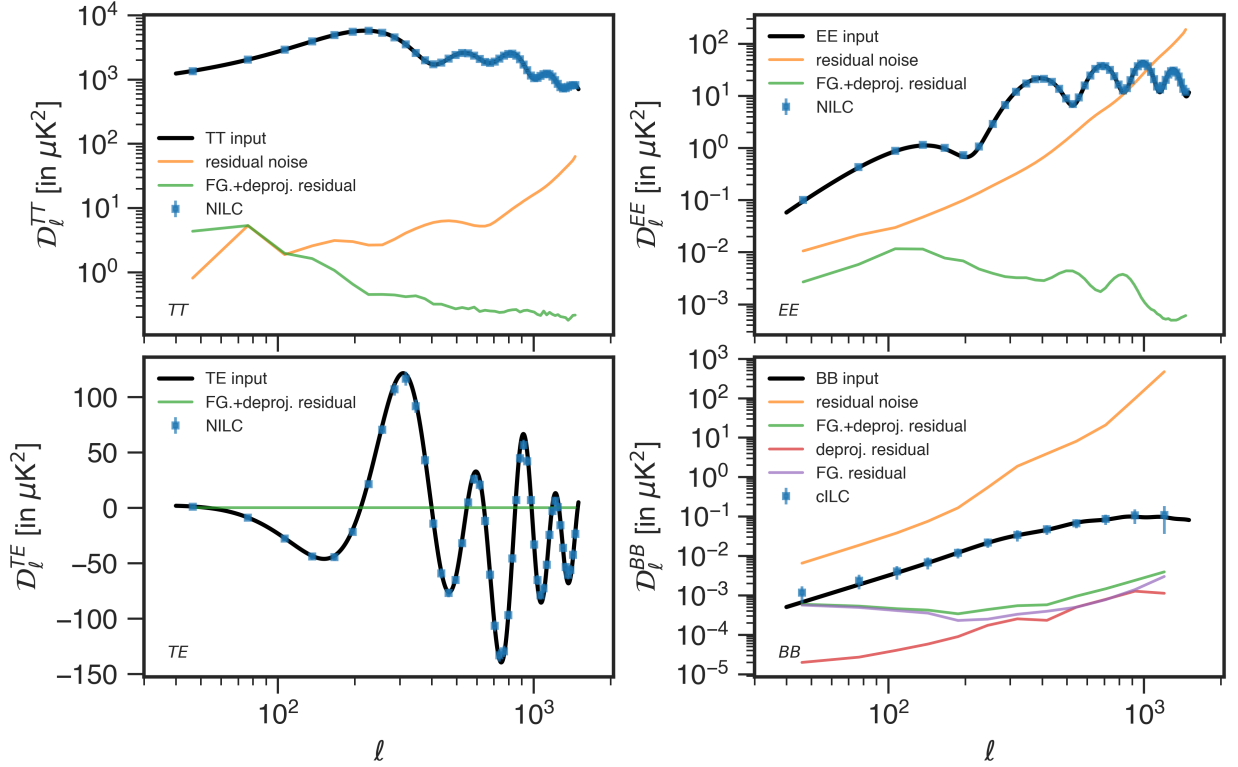


Fig. 7: Power spectra including NILC-cleaned TT (left top), NILC-cleaned EE (right top), NILC-cleaned TE (left bottom) and cILC-cleaned BB (right bottom) power spectra with $\ell_{\max} = 1500$. The input CMB (black solid curves), the reconstructed CMB (blue bars), the residual noise (orange curves) power spectra are plotted in each panel. The green curves represent the sum of the systematic and foreground residuals. For BB spectra, the deprojection and foreground residuals are separately shown in red and purple curves, respectively. The power spectra are binned over every 30 multipoles except for BB spectra, where a logarithm binning at $\ell > 100$ is adopted for clear display.

the Gaussian reconstruction noise sourced by the CMB and instrumental noise (N_0 bias) and the nonprimary couplings of the connected 4-point function (Kesden et al. 2003) (N_1 bias). In this study, the realization-dependent N_0 bias (RDN0) is calculated using 240 sets of simulation while the N_1 bias is calculated

analytically. After subtracting these biases, we obtain the final estimated power spectrum

$$\hat{C}_L^{\phi\phi} = \hat{C}_L^{\phi\phi} - \Delta C_L^{\phi\phi}|_{\text{RDN0}} - \Delta C_L^{\phi\phi}|_{N1}. \quad (14)$$

In Fig. 8, we show the reconstructed lensing potential power spectrum from polarization data, which combines EE , EB , and

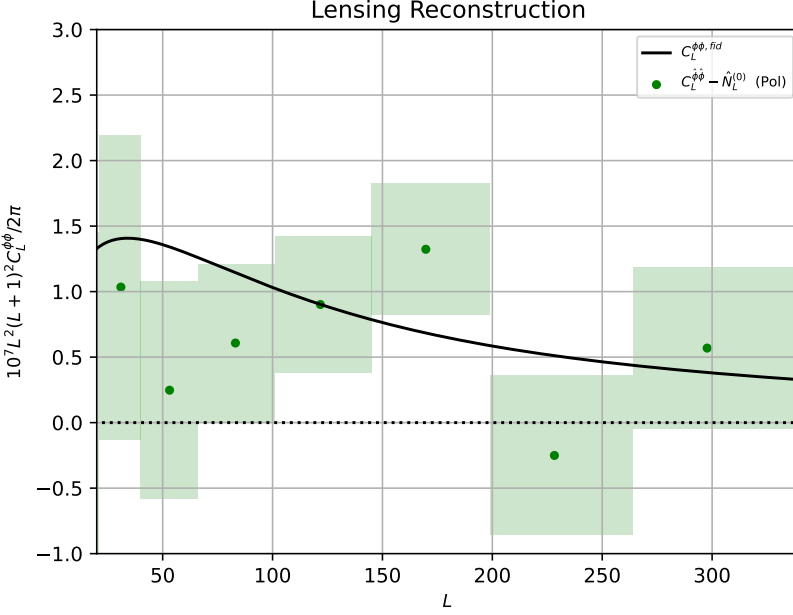


Fig. 8. Reconstructed lensing potential power spectrum from polarization estimator (green points). The colored boxes denote the 1σ error regions calculated from 240 sets of simulations.

BB estimators. The discrepancy in the figure between the reconstructed data point and theoretical prediction (black curve) is sourced by the Gaussian uncertainty of the single realization that represents the “real” data. Thus, it is expected that some of the data points may deviate by up to 1σ from the theoretical curve considering that each ℓ -bin is independent.

To evaluate our lensing reconstruction outcome, we estimated the signal-to-noise ratio (S/N) via the Fisher matrix method

$$S/N = \sqrt{\sum_{\ell, \ell'} C_{\ell} C_{\ell'}^{-1} C_{\ell'}}, \quad (15)$$

here the theoretical C_{ℓ} is used in the numerator rather than the reconstructed one to ensure a stable prediction. $C_{\ell\ell'}$ is the covariance matrix obtained from 240 simulation sets, which reads

$$C_{\ell\ell'} = \frac{1}{N-1} \sum_{n=1}^{N=240} \left[(\hat{C}_{\ell}^{\phi\phi} - \bar{C}_{\ell}^{\phi\phi}) \times (\hat{C}_{\ell'}^{\phi\phi} - \bar{C}_{\ell'}^{\phi\phi}) \right], \quad (16)$$

where $\bar{C}_{\ell}^{\phi\phi}$ is the averaged lensing potential power spectrum based on the simulation sets. The final S/N obtained from the multipole range of $\ell \in (20, 340)$ is about $S/N \approx 4.2$, this number is consistent with Han et al. (2023b), where we report a $S/N \approx 4.5$ with the same foreground removing and lensing reconstruction pipeline using a database with no systematics. Hence, we can conclude that the systematic residual does not contaminate the lensing reconstruction seriously.

4.5. Tensor-to-scalar ratio bias

In this section, we aim to estimate the bias on the tensor-to-scalar ratio r due to the beam systematic residual, by comparing the estimated r bias of the simulations with (after deprojection) and without the beam systematics.

We sample the posterior distribution of the tensor-to-scalar ratio r from the averaged cILC-cleaned *BB* power spectra by the

Markov Chain Monte Carlo (MCMC) analysis. We assume the Gaussian likelihood of r given the cleaned bandpowers \hat{C}_{ℓ_b} as:

$$-2 \ln \mathcal{L}(r) = \sum_{\ell_b, \ell_{b'}} \left[\hat{C}_{\ell_b} - r C_{\ell_b}^{r=1} - C_{\ell_b}^{\text{lens}} \right] \left[M_{\text{fid}}^{-1} \right]_{\ell_b, \ell_{b'}} \left[\hat{C}_{\ell_{b'}} - r C_{\ell_{b'}}^{r=1} - C_{\ell_{b'}}^{\text{lens}} \right], \quad (17)$$

where $\ell_b, \ell_{b'}$ are indices for multipole bins, $r C_{\ell_b}^{r=1} + C_{\ell_b}^{\text{lens}}$ refers to the theoretical binned *BB* power spectrum with a multipole range of $\ell \in [40, 200]$ including 5 ℓ_b 's, C_{ℓ}^{lens} is the *B*-mode spectrum due to gravitational lensing, $C_{\ell}^{r=1}$ is the *B*-mode spectrum sourced by tensor perturbations with $r = 1$, and $[M_{\text{fid}}]_{\ell_b, \ell_{b'}} = \langle (\hat{C}_{\text{fid}, \ell_b} - \langle \hat{C}_{\text{fid}, \ell_b} \rangle) (\hat{C}_{\text{fid}, \ell_{b'}} - \langle \hat{C}_{\text{fid}, \ell_{b'}} \rangle) \rangle$ is the fiducial covariance matrix computed from 300 systematic-free simulations. We derive the posterior distribution function assuming a uniform prior of $r \in [0, 1]$. We construct an MCMC chain consisting of 10,000 samples which satisfy the posterior distribution using the `emcee` (Foreman-Mackey et al. 2013) python package. We obtain the 1σ confidence interval (C.I.) and the 95% upper limit of r for both the deprojection and systematic-free cases.

The distribution of r is shown in Fig. 9. The resulting 1σ C.I. for the systematic-free case is $r = 0.019 \pm 0.013$ and the 95% C.I. is $r < 0.043$, while for the deprojection case the results are nearly the same. We note that in the selected scales $\ell \in [40, 200]$ where the *B*-mode spectrum is sensitive to tensor perturbations, the deprojection residual is negligible compared to the tensor power spectrum $C_{\ell}^{r=1}$ and foreground contaminants (see Fig. 7). Therefore, the beam systematics imprint negligible effects on the measurements of r .

5. Conclusions

In this paper, we forecast the systematic effects of beam mismatches on the forthcoming S3 observations. We adopt the deprojection technique in the mapmaking procedure to mitigate the $T \rightarrow P$ leakage induced by the random beam mismatches added to the S3 mock time-ordered data, and then assess the performance of deprojection on foreground cleaning, lensing

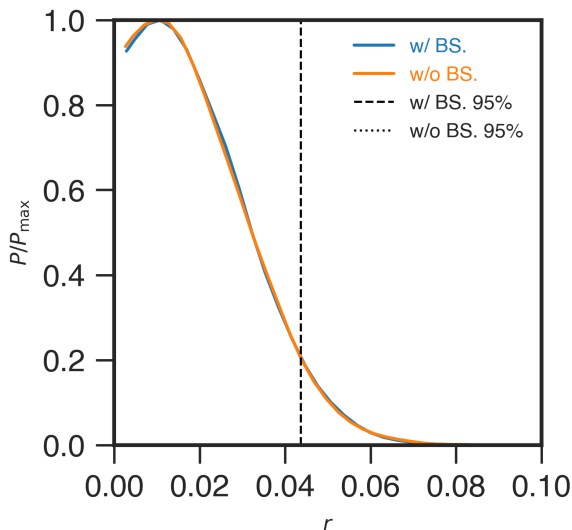


Fig. 9: Distribution of the tensor-to-scalar ratio for both cases with and without beam systematics. The dashed vertical lines represent the 95% upper bounds, which is 0.043 for both two cases.

reconstruction and r -estimation. First, we compare the CMB-plus-foregrounds after deprojection and the input CMB-plus-foregrounds without instrumental effects, in term of the TEB maps and the angular power spectra. The CMB and foregrounds are mixed up in deprojection thus unable to be separated from each other. We find the residual leakage can be ignored compared to the input CMB-plus-foregrounds.

Then, we impose the foreground cleaning methods, NILC for T/E modes and cILC for B modes, on the 300 simulations of seven frequency bands including S3 bands, Planck HFI bands and WMAP K band, where the S3 mock data are deprojected. The power spectrum of biases consisting of the residual $T \rightarrow P$ leakage and foregrounds, is shown to be negligible compared to the noise uncertainties for either TT , EE , TE or BB power. We evaluate the effect of beam systematics on the lensing reconstruction. Our lensing potential power spectrum reconstructed from the polarization estimator has a similar signal-to-noise ratio to that obtained in previous analysis without systematics, which demonstrates that the lensing reconstruction is almost unaffected by residual systematics. Finally, we set constraints on the tensor-to-scalar ratio r using the cleaned BB spectrum, where we obtain similar results with and without beam systematics, thanks to the deprojection technique that mitigates systematics to a negligible level. Our results justify the use of deprojection to filter the $T \rightarrow P$ leakage due to beam mismatches in S3 experiments, and safeness to ignore the residual leakage in the following data analysis pipeline. The effects of far sidelobes are not involved in this work since they are related to the specific shielding system of the telescope (BICEP2/Keck Collaboration et al. 2015) and the calibration or modeling of the realistic beam maps (Gallardo et al. 2018). The undeprojected residual due to differential beams of sidelobes will be calibrated in the future works.

Appendix A: PCL-TC Estimator

The $E \rightarrow B$ mixing is introduced when the partial-sky Q and U maps are converted to the E and B modes in harmonic space (Zhao & Baskaran 2010; Ghosh et al. 2021). We use the template cleaning method (Liu et al. 2019a,b) to get rid of the resulting $E \rightarrow B$ leakage. To estimate the full-sky B -mode power spectrum from foreground-cleaned maps, we adopt the pseudo- C_ℓ method to account for mode-coupling induced by masking and multipole binning using the NaMASTER (Alonso et al. 2019)⁶ package. The whole process is called the ‘‘PCL-TC’’ estimation.

The template cleaning method is a pixel-based technique to remove $E \rightarrow B$ leakage due to partial-sky effects. The steps are as follows:

1. First convert the masked (Q, U) maps into $(a_{\ell m}^E, a_{\ell m}^B)$ using the `map2alm` function of `healpy` (Zonca et al. 2019). Transform $a_{\ell m}^B$ into the B map being contaminated by the $E \rightarrow B$ leakage, B_c .
2. Convert the E -only modes $(a_{\ell m}^E, 0)$ back into maps (Q_E, U_E) using the `alm2map` function of `healpy`. Multiply them by the mask and convert them into $(a_{\ell m}^{E'}, a_{\ell m}^{B'})$ using `map2alm`. The B map derived from $a_{\ell m}^{B'}$ is taken as our $E \rightarrow B$ leakage template, B_t .
3. Linearly fit the masked leakage template B_t to the masked contaminated map B_c in the pixel space. Finally subtract the fitted leakage to obtain the pure B -mode map: $B_{\text{pure}} = B_c - \alpha B_t$, where α is the linear coefficient.

Deprojection, as any other filtering operation on Q and U time streams, can produce a small amount of $E \rightarrow B$ mixing. The $E \rightarrow B$ leakage due to deprojection could also be corrected for by taking advantage of deprojected E -mode only data to get a B -mode leakage template (see Sect. 4.2 of Ghosh et al. (2022)).

After the foreground cleaning, we correct for the common beam (11 arcmin) and pixel window functions in the $a_{\ell m}$'s. Finally we compute the full-sky bandpowers with a bin size of 30 using the `decouple_cell` module of `pymaster`.

Acknowledgements. We thank Zirui Zhang, Siyu Li and Jing Jin for helpful discussions. This work is supported by the National Key R&D Program of China Grant No. 2021YFC2203102, 2020YFC2201603, NSFC No. 12325301 and 12273035. Jiakang Han thanks Stefano Camera for various support for this project. Some of the results in this paper have been derived using the `pymaster`, `emcee`, `healpy`, and `HEALPix` packages.

References

Abazajian, K., Abdulghafour, A., Addison, G. E., et al. 2022, ArXiv e-prints [arXiv:2203.08024]
 Abazajian, K. N., Adshead, P., Ahmed, Z., et al. 2016, CMB-S4 Science Book, First Edition
 Alonso, D., Sanchez, J., & Slosar, A. 2019, Mon. Not. R. Astron. Soc., 484, 4127
 Basak, S. & Delabrouille, J. 2012, Mon. Not. R. Astron. Soc., 419, 1163
 Basak, S. & Delabrouille, J. 2013, Monthly Notices of the Royal Astronomical Society, 435, 18
 Bennett, C. L., Larson, D., Weiland, J. L., et al. 2013, ApJS, 208, 20
 BICEP2 Collaboration, Ade, P., Aikin, R., Amiri, M., et al. 2014, Astrophys. J., 792, 62
 BICEP2 Collaboration, Ade, P. A. R., Aikin, R. W., et al. 2015, Astrophys. J., 814, 110
 BICEP2/Keck Collaboration, Ade, P. A. R., Aikin, R. W., et al. 2015, Astrophys. J., 806, 206
 BICEP/Keck Collaboration, Ade, P. A. R., Ahmed, Z., et al. 2021, Phys. Rev. Lett., 127, 151301
 BICEP/Keck Collaboration, Ade, P. A. R., Ahmed, Z., et al. 2023, Astrophys. J., 949, 43

Blanchard, A. & Schneider, J. 1987, Astron. Astrophys., 184, 1
 Carron, J. & Lewis, A. 2017, Phys. Rev. D, 96, 063510
 CMB-S4 Collaboration, Abazajian, K., Addison, G. E., et al. 2022, Astrophys. J., 926, 54
 Delabrouille, J., Betoule, M., Melin, J.-B., et al. 2013, Astron. Astrophys., 553, A96
 Delabrouille, J., Cardoso, J.-F., Jeune, M. L., et al. 2009, Astron. Astrophys., 493, 835
 Dou, J., Ghosh, S., Santos, L., & Zhao, W. 2024, JCAP, 05, 006
 Foreman-Mackey, D., Hogg, D. W., Lang, D., & Goodman, J. 2013, Publications of the Astronomical Society of the Pacific, 125, 306
 Gallardo, P. A., Cothard, N. F., Puddu, R., et al. 2018, in Millimeter, Submillimeter, and Far-Infrared Detectors and Instrumentation for Astronomy IX, ed. J. Zmuidzinas & J.-R. Gao, Vol. 10708, International Society for Optics and Photonics (SPIE), 107082L
 Ghosh, S., Delabrouille, J., Zhao, W., & Santos, L. 2021, JCAP, 2021, 036
 Ghosh, S., Liu, Y., Zhang, L., et al. 2022, JCAP, 10, 063
 Gorski, K. M., Hivon, E., Banday, A. J., et al. 2005, Astrophys. J., 622, 759
 Han, J., Cao, Y., & Hu, B. 2023a, Scientia Sinica: Physica, Mechanica et Astronomica, 53
 Han, J., Hu, B., Ghosh, S., et al. 2023b, JCAP, 04, 063
 Harrington, K., Marriage, T., Ali, A., et al. 2016, in Millimeter, Submillimeter, and Far-Infrared Detectors and Instrumentation for Astronomy VIII, ed. W. S. Holland & J. Zmuidzinas (SPIE)
 Hazumi, M., Ade, P. A. R., Akiba, Y., et al. 2019, J Low Temp Phys, 194, 443
 Hu, W. 2001, Astrophys. J. Lett., 557, L79
 Hu, W., Hedman, M. M., & Zaldarriaga, M. 2003, Physical Review D, 67 [astro-ph/0210096]
 Hu, W. & Okamoto, T. 2002, Astrophys. J., 574, 566
 Kesden, M., Cooray, A., & Kamionkowski, M. 2003, Phys. Rev. D, 67, 123507
 Lewis, A., Challinor, A., & Lasenby, A. 2000, Astrophys. J., 538, 473
 Li, H., Li, S.-Y., Liu, Y., Li, Y.-P., & Zhang, X. 2018, Nature Astron., 2, 104
 Li, H. et al. 2019, Natl. Sci. Rev., 6, 145
 Liu, H., Creswell, J., & Dachlythra, K. 2019a, JCAP, 2019, 046
 Liu, H., Creswell, J., von Hausegger, S., & Naselsky, P. 2019b, Phys. Rev. D, 100, 023538
 Liu, J., Han, J., & Hu, B. 2022a, Scientia Sinica: Physica, Mechanica et Astronomica, 52
 Liu, J., Sun, Z., Han, J., et al. 2022b, Sci. China Phys. Mech. Astron., 65, 109511
 Louis, T., Grace, E., Hasselfield, M., et al. 2017, JCAP, 06, 031
 Maniyar, A. S., Ali-Haïmoud, Y., Carron, J., Lewis, A., & Madhavacheril, M. S. 2021, Phys. Rev. D, 103, 083524
 Mennella, A., Ade, P., Amico, G., et al. 2019, Universe, 5, 42
 Okamoto, T. & Hu, W. 2003, Phys. Rev. D, 67, 083002
 Planck Collaboration, Aghanim, N., Akrami, Y., et al. 2019, Planck 2018 Results. VIII. Gravitational Lensing
 Planck Collaboration, Aghanim, N., Akrami, Y., Ashdown, M., et al. 2020a, Astron. Astrophys., 641, A6
 Planck Collaboration, Aghanim, N., Ashdown, M., et al. 2016, Astron. Astrophys., 596, A109
 Planck Collaboration, Akrami, Y., Andersen, K. J., et al. 2020b, Astron. Astrophys., 643, A42
 Planck Collaboration, Akrami, Y., Ashdown, M., et al. 2020c, Astron. Astrophys., 641, A4
 Reinecke, M., Belkner, S., & Carron, J. 2023, Astron. Astrophys., 678, A165
 Remazeilles, M., Delabrouille, J., & Cardoso, J.-F. 2011, Mon. Not. R. Astron. Soc., 410, 2481
 Remazeilles, M., Rotti, A., & Chluba, J. 2021, Mon. Not. Roy. Astron. Soc., 503, 2478
 Sayre, J. T., Reichardt, C. L., Henning, J. W., et al. 2020, Phys. Rev. D, 101, 122003
 Sheehy, C. 2019, arXiv:1911.03547 [astro-ph.IM] [arXiv:1911.03547]
 Simons Observatory Collaboration, Ade, P., Aguirre, J., et al. 2019, JCAP, 2019, 056
 Tristram, M., Banday, A. J., Gorski, K. M., et al. 2022, Phys. Rev. D, 105, 083524
 Zaldarriaga, M. & Seljak, U. 1998, Phys. Rev. D, 58, 023003
 Zhao, W. & Baskaran, D. 2010, Phys. Rev. D, 82, 023001
 Zonca, A., Singer, L., Lenz, D., et al. 2019, Journal of Open Source Software, 4, 1298

⁶ <https://github.com/LSSDESC/NaMaster>